e-Proceedings

TMETC 15th Thailand Metallurgy Conference & TCPC2025

The 5th International Thailand Corrosion Prevention and Control Conference

Academic-Industrial Linkage Towards Innovative Metallurgy & Emerging Applications

Co-located with METALEX 2025

November 20-21, 2025

Bangkok International Trade & Exhibition Centre (BITEC), Bangkok, THAILAND

Diamond Sponsors

JST Innovation & Excellence | posco THAINOX | THAI TORAY THERMO

Gold Sponsors

outokumpu sustainable stainless steel | ThaiPMA

Exhibitors & Supporters

igs | hju | fischer | THAI PARKERIZING | TMP | Metrohm Siam Ltd. | KEYENCE | COAX | Minitab AUTHORIZED PARTNER | SOLUTION CENTER

https//:www.mtec.or.th/tmetc15
https//:www.mtec.or.th/tcpc2025

Table of Contents

The 15th Thailand Metallurgy Conference (TMETC-15)
The 5th International Thailand Corrosion Prevention

20-21 November 2025 at BITEC Bangkok, THAILAND

Technical Program

DAY I	Thursday, 20 November 2025
Session	**TCMA Awards**
Session Chair	Asst. Prof. Dr. Chaiyasit Banjongprasert, Chiang Mai University
15:30 - 15:50	**A-O-12** **The effect of temperature on corrosion of bismuth-40tin alloys in 3.5 wt.% NaCl solution** **Chanin Tangpongkitjaroen** Department of Metallurgical Engineering, Faculty of Engineering, Chulalongkorn University

The effect of temperature on corrosion of bismuth-40tin alloys in 3.5 wt.% NaCl solution

Chanin Tangpongkitjaroen[1], Tachai Luangvaranunt[1], Patama Visuttipitukul[1], Suwin Sompopsart[2], Wararit Toempromaraj[2], Passaworn Silakorn[2], Kittithuch Hnuruang[2], and Pitichon Klomjit[1,]*

[1] Department of Metallurgical Engineering, Faculty of Engineering, Chulalongkorn University, Bangkok 10330, Thailand
[2] PTT Exploration and Production Public Company Limited
***Corresponding author:** Pitichon.K@chula.ac.th

Abstract. The alternative plugging and abandonment (P&A) protocol utilizing thermite technology has attracted considerable attention in the oil and gas industry. By employing a thermite heater, low-melting-point alloys can be melted to seal the wellbore upon solidification, thereby preventing the leakage of chemical substances from the downhole. Bismuth–40 wt.% tin alloy (Bi-40Sn) is a promising candidate for P&A applications due to its low melting point, good castability, and expansion upon solidification, which enhances the sealing performance of the alloy plug. However, the corrosion of the alloy may significantly affect its mechanical properties, limiting its long-term use as a plug material. Furthermore, temperature and chloride ions are known to have a substantial influence on the corrosion rate of such alloys. In this study, the effect of temperature on the corrosion behavior of Bi-40Sn alloy in a 3.5 wt.% NaCl solution was investigated. The result from electrochemical method revealed that temperature had a pronounced influence on the corrosion of Bi-40Sn in 3.5 wt.% NaCl solution. At 25 °C, the alloy maintained a stable passive film, producing a single Nyquist semicircle indicative of a corrosion process governed by one interfacial reaction. As the temperature increased to 60 °C and 90 °C, chloride ions more readily penetrated and degraded the passive layer, resulting in two distinct charge-transfer processes and reflecting more aggressive corrosion kinetics at elevated temperatures. FESEM analysis supported these electrochemical findings. The unexposed alloy exhibited a lamellar eutectic microstructure, with Bi-rich and Sn-rich phases clearly distinguished. Post-corrosion morphologies showed preferential dissolution of the Sn-rich phase at all temperatures due to the potential difference between Bi and Sn, confirming selective-leaching as a dominant degradation mechanism. The severity of Sn depletion intensified at higher temperatures, demonstrating that increased temperature accelerates selective-leaching and overall alloy deterioration. These results collectively suggest that the long-term stability of Bi-40Sn in chloride-rich downhole environments is strongly temperature dependent.

Graphical abstracts

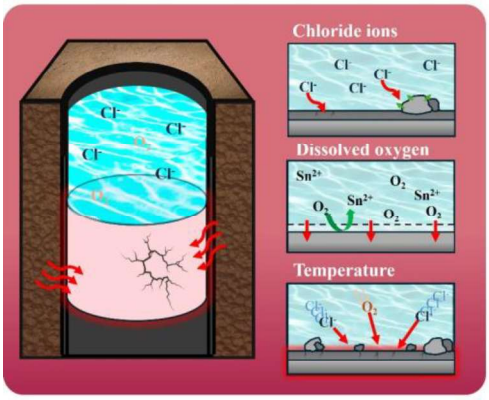

1 Introduction

Petroleum drilling underpins the exploration and production of hydrocarbon resources. When exploratory wells are non-productive or when reservoirs are depleted, permanent well abandonment (P&A) is required to prevent the migration of fluids and chemicals from the wellbore into surrounding formations, which can harm nearby ecosystems. This operation, however, is both time-intensive and expensive. In addition, cement, which is the plug materials for conventional P&A, can exhibit limited compatibility with downhole conditions, increasing the risk of degradation over time [1]. These challenges highlight the need for improved technologies and alternative plugging materials tailored for robust and durable well abandonment.

Recent studies have explored alternative plug and abandonment (P&A) approaches, including the use of thermite-based technologies [2–4]. The heat generated by thermite heaters can melt low–melting point metals, enabling their injection into the wellbore as sealing materials. Bismuth-tin alloys have gained attention for this purpose, often in combination with cement, due to their low melting temperature, solidification-induced volume expansion, and resistance to corrosive downhole fluids and gases. However, the corrosion of bismuth-tin alloys under downhole conditions which affect the durability of plug remains insufficiently understood and continues to be an important research focus.

This study investigates the influence of temperature on corrosion of a bismuth–tin alloy containing 40 wt.% Sn (Bi-40Sn) in a 3.5 wt.% NaCl solution. The aim is to assess how geothermal-level temperatures and chloride-rich brine environments influence the long-term durability of Bi-40Sn when used as a plugging material in P&A applications.

2 Experimental procedure

2.1 Sample preparation

The Bi–40Sn alloys used in this study were prepared by casting. High-purity bismuth (99.99%) and tin (99.9%) were combined at a weight ratio of 60:40 and melted on a hotplate. The molten mixture was then cast into plate shape with dimensions of 20 × 20 × 2 mm. The as-cast samples were ground sequentially using silicon carbide sandpapers from #400 to #1200, rinsed with ethanol, dried with a hair dryer, and finally stored in a desiccator overnight.

2.2 Electrochemical testing

Electrochemical testing was performed to investigate the corrosion behavior of the Bi–40Sn alloy at different temperatures. Bi–40Sn samples served as the working electrode in a three-electrode setup, with Ag/AgCl as the reference electrode and platinum as the counter electrode. The experiments were conducted in 3.5 wt.% NaCl solution at temperatures of 25, 60, and 90 °C, controlled using a hotplate with a temperature-controlled system (MSH-20D, DAIHAN) with accuracy of ± 1°C. A PGSTAT204 electrochemical workstation (AUTOLAB) was used for all measurements.

The open-circuit potential (OCP) was recorded for 30 minutes after immersing the specimens in the solution. Subsequently, electrochemical impedance spectroscopy (EIS) was conducted over a frequency range of 10^{-1} to 10^{4} Hz with a sinusoidal amplitude of 0.01 V_{RMS}, using 10 data points per cycle. Equivalent circuit fitting was performed using NOVA software.

Potentiodynamic polarization (PL) measurements were carried out from the cathodic to the anodic direction at a scan rate of 0.167 mV/s, ranging from −50 mV to +100 mV versus OCP. Tafel extrapolation was performed using NOVA software. After PL testing, the specimens were rinsed thoroughly with deionized water several times, dried with a hair dryer, and kept in desiccator.

2.3 Material characterization

The corrosion morphology of Bi–40Sn alloys before and after PL testing at different temperatures was further investigated using a field-emission scanning electron microscope (FESEM, Quanta 250 FEG).

3 Result and discussion

3.1 Electrochemical testing

Electrochemical testing was performed to examine the effect of temperature on the corrosion behavior of Bi–40Sn alloys in 3.5 wt.% NaCl solutions at 25, 60, and 90 °C, as shown in Fig. 1. The OCP monitoring results indicate that the OCP of Bi–40Sn alloys decreases significantly with increasing temperature, suggesting that higher temperatures enhance the electrochemical activity of the alloys in the corrosive environment. However, it should be noted that OCP values do not directly correlate with the corrosion rate of the alloys.

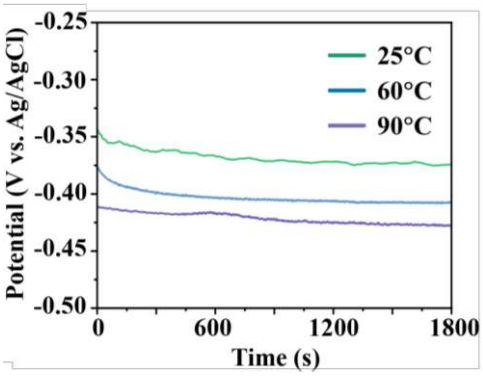

Fig. 1 OCP monitoring of Bi-40Sn in 3.5 wt.% NaCl solution at different temperatures.

PL was applied to investigate the corrosion behavior of Bi–40Sn alloys at different temperatures, as shown in Fig. 2. The corresponding parameters from PL analysis are summarized in Table 1. The results indicate that the corrosion rate of the alloys increases significantly with temperature, rising from 58.43 to 308.15 and 1434.7 µm/yr at 25, 60, and 90 °C, respectively. Additionally, the cathodic current at 60 °C and 90 °C increased by an order of magnitude compared to 25 °C, suggesting an accelerated cathodic reaction, primarily due to enhanced oxygen reduction at higher temperatures.

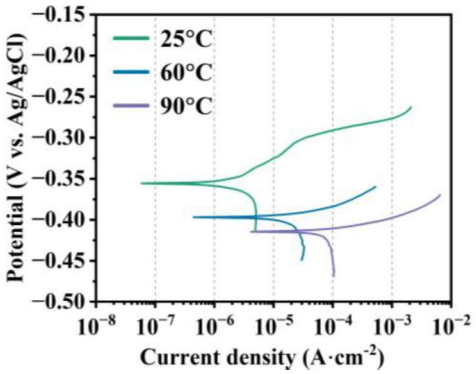

Fig. 2 Polarization curve of Bi-40Sn in 3.5 wt.% NaCl solution at different temperatures.

Table 1 Corresponding corrosion parameters from Tafel extrapolation

T (°C)	Corrosion rate (µm/year)	E_{corr} (V)	R_p (Ω)	|ba| (mV/dec)	|bc| (mV/dec)
25	58.43	-0.36	5310	46.84	75.51
60	308.15	-0.37	398.4	15.34	44.91
90	1434.7	-0.41	83.62	13.10	76.15

EIS study was conducted to evaluate the corrosion behavior of the alloys. As shown in Fig. 3a, the Nyquist plot at 25 °C displayed a single semicircle, indicating that the corrosion process is governed primarily by the solid–electrolyte interface. In contrast, at elevated temperatures of 60 °C and 90 °C, two semicircles were observed, suggesting that the corrosion process involves both the passive film–electrolyte interface and the solid–electrolyte interface. These results indicate that a stable passive film can retard corrosion at lower temperatures, whereas at higher temperatures, chloride ions can penetrate and degrade the film, leading to an additional charge-transfer process and the dual semicircle response observed.

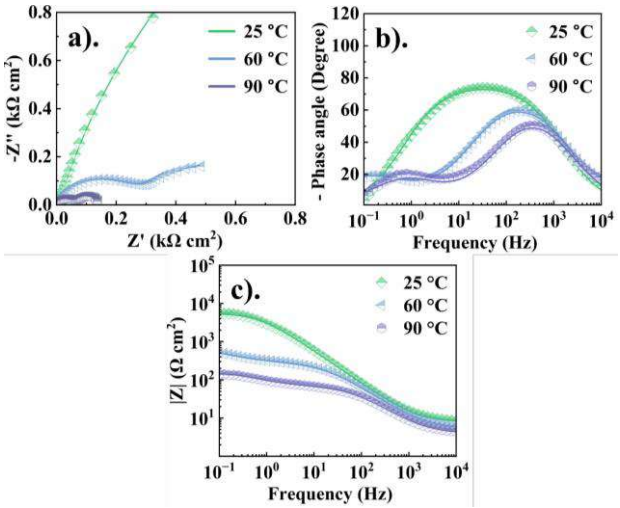

Fig. 3 Electrochemical impedance spectrum of Bi-40Sn alloys in 3.5 wt.% NaCl solution with different temperatures: (a) Nyquist plot, bode plot of (b) phase angle and (c) modulus plot

Furthermore, an equivalent electrical circuit model was applied to estimate the film resistance (R_f) and charge transfer resistance (R_{ct}) of Bi–40Sn at different temperatures. The electrochemical circuit used for the analysis is shown in Fig. 4. A simple Randles circuit was applied to the EIS data at 25 °C, whereas for 60 and 90 °C, a Randles circuit with an inner loop was employed to simulate the breakdown of the passive film. The results of the circuit fitting are presented in Table 2. The polarization resistance (R_p), defined as the sum of R_{ct} and R_f, decreased rapidly with increasing temperature, from 5613 Ω·cm² at 25 °C to 903.9 Ω·cm² and 157.4 Ω·cm² at 60 and 90 °C, respectively. These results clearly demonstrate the diminished protective ability and result in high corrosion rate of the Bi–40Sn alloy at elevated temperatures.

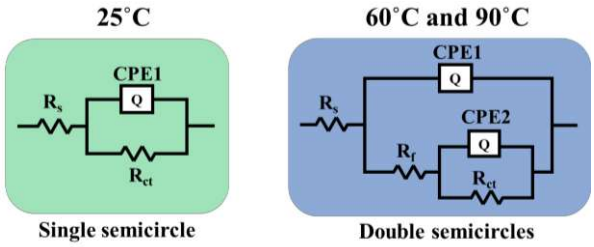

Fig. 4 Corresponding electrochemical equivalent circuit for electrochemical circuit models.

Table 2 Corresponding parameters from equivalent circuit analysis of EIS results with different temperatures.

T (°C)	R_s (Ω · cm²)	CPE1 (S · sec^n)	n_2	R_f (Ω · cm²)	CPE2 (S · sec^n)	n_2	R_{ct} (Ω · cm²)	R_p (Ω · cm²)
25	8.021	4.99×10^{-5}	0.85	-	-	-	5613	5613
60	5.378	8.32×10^{-5}	0.81	275.1	362.2×10^{-5}	0.63	628.8	903.9
90	3.858	13.1×10^{-5}	0.8	66.47	592.2×10^{-5}	0.75	90.89	157.4

The results from the electrochemical circuit fitting were consistent with the Bode phase shift plots shown in Fig. 3b, where the maximum phase angle of the Bi–40Sn alloy reached 75° at 25 °C and decreased to 60° and 50° at 60 °C and 90 °C, respectively. Furthermore, the Bode impedance plot in Fig. 3c demonstrates a decrease in modulus impedance at 0.1 Hz with increasing temperature. These observations indicate that the passive film or corrosion product layers on the alloy surface progressively lose their protective ability as temperature rises. Additionally, the solution resistance (R_s) decreased from 8.021 Ω·cm² at 25 °C to 5.378 Ω·cm² and 3.858 Ω·cm² at 60 °C and 90 °C, respectively, suggesting enhanced ionic conductivity at higher temperatures [5]. This increase in conductivity is attributed to the weakening of intermolecular bonds in water with rising temperature, which accelerates the oxygen reduction reaction and reduces the overall corrosion resistance of the alloy [6].

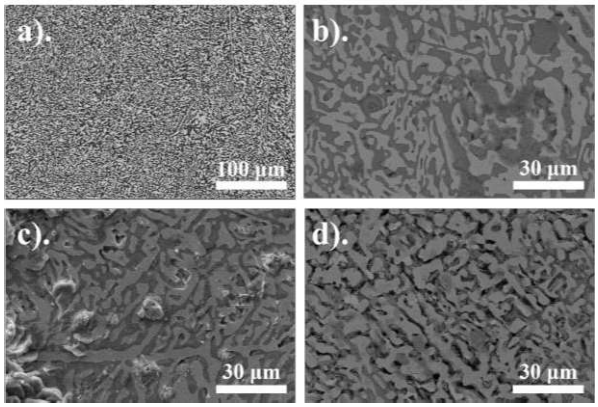

Fig. 5 FESEM images of the Bi-40Sn alloy: (a) before testing, and after potentiodynamic polarization at (b) 25 °C, (c) 60 °C, and (d) 90 °C.

Furthermore, the corrosion morphology of Bi–40Sn alloys after potentiodynamic polarization was examined using FESEM. As shown in Fig. 5a, the Bi–40Sn alloy exhibits a lamellar microstructure characteristic of eutectic alloys, with the brighter regions corresponding to the Bi-rich phase due to its higher atomic number. The post-corrosion morphologies at 25 °C, 60 °C, and 90 °C are presented in Fig. 5b, Fig. 5c, and Fig. 5d, respectively. The depletion of the Sn-rich phase was observed after electrochemical testing, indicating selective-leaching corrosion [7-8]. This behavior arises from the significant potential difference between bismuth (+0.50 V vs. SHE) and tin (−0.138 V vs. SHE). When electrically connected within the microstructure, electrons flow from the less noble Sn-rich phase to the more noble Bi-rich phase, promoting cathodic activity at the Bi-rich phase and preferential anodic dissolution of the Sn-rich phase. Moreover, the severity of selective-leaching corrosion increases with temperature, indicating that higher temperatures accelerate the preferential dissolution of Sn, which is consistent with the results from potentiodynamic polarization measurements.

4 Conclusion

In this study, the effect of temperature on corrosion of Bi-40Sn alloys was investigated. The result indicates that temperature plays a critical role in governing the corrosion degradation of such alloys. As temperature increases, the corrosion rate rises due to accelerated electrochemical kinetics, enhanced dissolution of the Sn-rich phase, and reduced stability of the passive film. Elevated temperatures also intensify selective-leaching corrosion, resulting in more pronounced depletion of tin-rich phase. Overall, higher temperatures significantly reduce the corrosion resistance of Bi-40Sn alloy and promote more severe degradation mechanisms.

Declaration of Competing Interest

The authors declare no known competing financial interests or personal relationships that could have influenced the work reported in this paper.

Acknowledgement

We would like to acknowledge PTT Exploration and Production (PTTEP) and Department of Metallurgical Engineering, Chulalongkorn University, for financial support. We would also like to thank the ChatGPT for its support in language editing and improving the clarity of this research.

References

[1] L. Hmadeh, M.A. Jaculli, B. Elahifar, S. Sangesland, Petroleum Research 9(2) (2024) 250–264. **DOI:** 10.1016/j.ptlrs.2024.01.003

[2] P. Carragher, J. Fulks, SPE ATCE (2018) D011S001R006. **DOI:** 10.2118/191469-MS.

[3] H. Zhang, T. Ramakrishnan, Q.K. Elias, A. Jr. Perez, SPE Prod. Oper. 35(1) (2020) 111–124. **DOI:** 10.2118/199363-PA.

[4] H. Zhang, T. Ramakrishnan, Y.M. Elkady, Y. Feng, Q.K. Elias, SPE Drill. Complet. 36(2) (2021) 368–382. **DOI**: 10.2118/202488-PA.

[5] M. Wang, J. Wang, H. Feng, W. Ke, J. Mater. Sci.: Mater. Electron. 23 (2012) 148–155. **DOI:** 10.1007/s10854-011-0552-1.

[6] C. Qiao, M. Wang, L. Hao, X. Liu, X. Jiang, X. An, D. Li, J. Mater. Sci. Technol. 75 (2021) 252–264. **DOI:** 10.1016/j.jmst.2020.11.012.

[7] Mostofizadeh, M.; Pippola, J.; Marttila, T.; Frisk, L.K. IEEE Trans. Components, Packag. Manuf. Technol. 3(10) (2013) 1778–1785. **DOI:** 10.1109 /TCPMT.2013.2267333.

[8] M. Mori, K. Miura, T. Sasaki, T. Ohtsuka, Corros. Sci. 44(4) (2002) 887–898. **DOI:** 10.1016/S0010-938X(01)00094-4.

The 15th Thailand Metallurgy Conference (TMETC-The 5th International Thailand Corrosion

20-21 November 2025 at BITEC Bangkok, THAILAND

Technical Program

DAY I	Thursday, 20 November 2025
Session	**Manufacturing & Process Industries III**
Session Chair	Assoc. Prof. Dr. Wantanee Buggakupta, Chulalongkorn Univerysity
15:50 - 16:10	**C-O-4** **Fabrication of Aluminium Foams Using Coated and Uncoated Oyster Shell Foaming Agents** **Laksika Usuwan** Department of Metallurgical Engineering, Faculty of Engineering, Chulalongkorn University

Fabrication of Aluminium Foams Using Coated and Uncoated Oyster Shell Foaming Agents

Laksika Usuwan [1], *Sirichai* Leelachao [2], and *Seksak* Asavavisithchai [3*]

[1]Department of Metallurgical Engineering, Faculty of Engineering, Chulalongkorn University, Bangkok 10330, Thailand.
***Corresponding author:** seksak.a@chula.ac.th

Abstract. Closed-cell aluminium foam has garnered significant attention for structural applications due to its low density, high strength-to-weight ratio, excellent stiffness, and superior energy absorption capacity. Traditionally, such foams are fabricated using foaming agents like metal hydrides or carbonates. Among these, carbonate-based foaming agents are favored for their lower toxicity, ease of handling, cost-effectiveness, and ability to produce foams with fine and uniform cell structures. In this study, oyster shell powder, rich in calcium carbonate ($CaCO_3$), was employed as a sustainable and low-cost foaming agent at concentrations of 3 wt.% and 5 wt.% to produce ADC12 aluminium foams. The influence of surface modification of the oyster shell powder with sodium fluoride (NaF) on foam expansion behavior was systematically investigated. Axial compression tests were conducted to evaluate the mechanical performance of the resulting foams. The experimental results indicate that the use of 5 wt.% NaF-coated oyster shell powder yields the highest foam expansion and leads to the formation of a more homogeneous and refined pore structure. This finding highlights the potential of modified biogenic carbonate sources as effective and eco-friendly alternatives for aluminium foam production.

Graphical abstracts

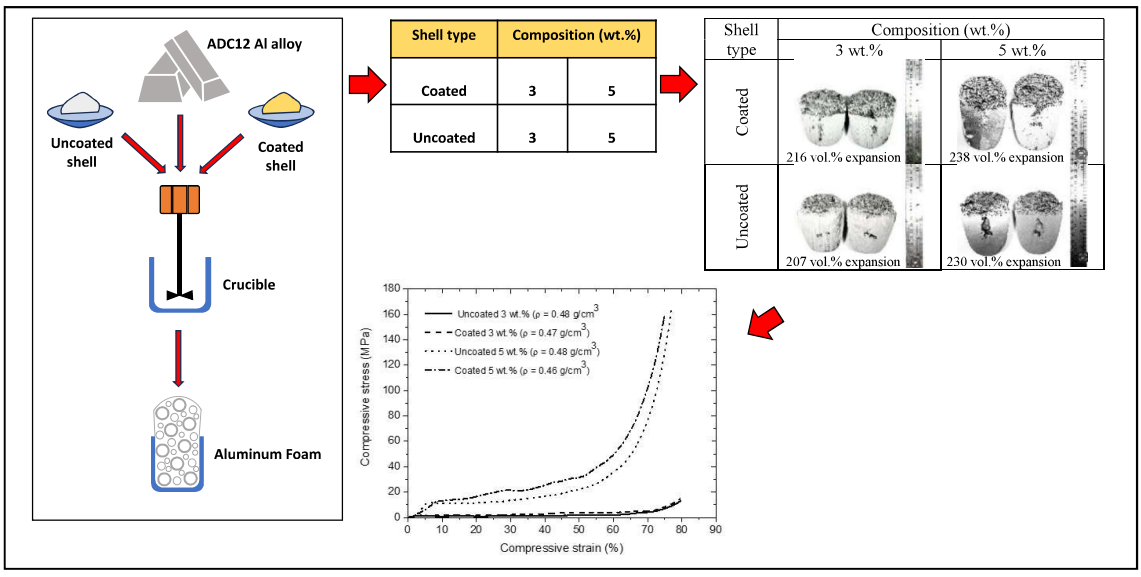

1 Introduction

Aluminium (Al) foams are an emerging class of lightweight materials, offering a unique combination of structural efficiency and functional properties. The closed-cell variant of Al foam, in particular, is valued for its high specific strength and stiffness, low thermal conductivity and excellent energy absorption capability, making it suitable for automotive crash components, aerospace structures and protective systems [1, 2]. Among production methods, the melt route process remains the most industrially relevant fabrication technique, involving the incorporation of foaming agents into a molten Al alloy matrix [3]. Upon decomposition, the foaming agents release gases, generating pores that stabilise into the cellular structure during solidification. Among various agents, calcium carbonate ($CaCO_3$) is widely used, due to its low toxicity, low cost and favorable decomposition characteristics [4]. However, challenges remain in controlling the uniformity of pore nucleation and the timing of gas release.

Oyster shells, composed primarily of $CaCO_3$ in the aragonite and calcite phases, are an abundant biogenic waste material that can serve as a sustainable source of foaming agents [5]. Their use not only promotes circular economy practices, but also reduces environmental burden from aquaculture waste. Nonetheless, unmodified oyster shell powder may suffer from inconsistent decomposition and poor wettability with molten Al. Surface modification, such as coating with salts or fluorides, has been reported to improve decomposition behavior and enhance foam uniformity [6]. Sodium fluoride (NaF) in particular can lower decomposition onset temperature and promote better interfacial reactions between the carbonate particles and molten Al.

In this study, oyster shell powder was investigated as a foaming agent for ADC12 Al alloy, a die-cast grade alloy widely used in automotive and structural components. Both uncoated and NaF-coated oyster shell powders were introduced at two concentrations (3 wt.% and 5 wt.%) into the molten alloy during melt foaming. The effects on foam expansion, macrostructure, microstructure and compressive properties were systematically compared. The results highlight the role of NaF coating and powder loading on pore morphology and mechanical performance.

2 Experimental procedure

ADC12 Al alloy ingots, supplied by MetalCom, were used as the matrix. Oyster shells were collected, cleaned and dried at 100 °C for 1 h to remove organic residues. The dried shells were ground into powders and sieved to <210 µm. For surface modification, powders were coated with NaF by immersion in a 0.1 M aqueous NaF solution, followed by filtration and drying at 120 °C [6]. Characterisation of shell foaming agent was performed with MALVERN Mastersizer 3000 laser particle size distribution (PSD) analyser, Simultaneous Thermal Analysis (STA) NETZSCH STA 449 F3 Jupiter to examine decomposition temperature and gas evolution.

Al foams were produced via the melt route. ADC12 ingots were melted in a graphite crucible at 700 °C. Oyster shell powders, either uncoated or NaF-coated, were added at 3 wt.% and 5 wt.% relative to the melt mass. After mechanical stirring at 300 rpm for 2 min, the furnace temperature was increased to 750°C and held for 15 min to initiate and sustain foaming expansion. After the expansion phase, the foamed samples were removed from the furnace and allowed to solidify in air. The solidified samples were then longitudinally sectioned for subsequent macrostructural and microstructural characterisation, and mechanical testing. The ImageJ software was employed to perform quantitative image analysis of the cell structures.

Microstructural evaluation of the foam samples was carried out following standard metallographic preparation procedures for Al alloys. Sectioned specimens were ground, polished, and observed under an optical microscope. The JEOL JSM-IT300 scanning electron microscope (SEM), which was equipped with energy dispersive X-ray spectroscopy (EDS) for qualitative phase analysis, was employed to examine the morphology of oyster shell powder. Axial compression tests were performed to evaluate the mechanical performance of the fabricated foams. Cubic specimens (20 mm × 20 mm × 20 mm) were prepared from the central region of the foamed blocks. Testing was conducted using a Shimadzu AG-X Plus universal testing machine at a constant strain rate of 0.01 mm/s, under quasi-static conditions. From the resulting stress–strain curves, both compressive strength and energy absorption capacity were calculated.

3 Results and discussion

Fig. 1 displays the morphology of uncoated and coated oyster shell powders. The uncoated powders reveal irregularly shaped particles with angular morphologies and relatively rough surfaces. The surface texture of the uncoated powders appears porous and uneven, which is characteristic of natural biogenic $CaCO_3$ derived from oyster shells. In contrast, the NaF-coated oyster shell powders exhibit notable morphological differences. The particles show more compact and refined shapes, with a comparatively smoother and denser surface layer. The coating appears to form a continuous and adherent layer on the shell particle surface, effectively masking the underlying porous microstructure. The PSD analysis revealed a mean particle diameter of 217.34 µm, with corresponding D_{10}, D_{50}, and D_{90} values of 19.67 µm, 175.12 µm, and 466.09 µm, respectively.

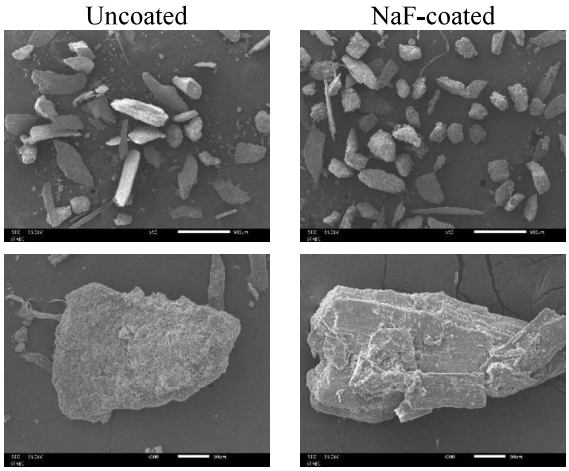

Fig. 1. SEM micrographs showing morphology and distribution of uncoated and coated oyster shell powders.

Fig. 2 presents the simultaneous thermal analysis (STA) results of coated and uncoated oyster shell powders, showing both mass change (TG) and differential thermal analysis (DTA) curves as a function of temperature. Both samples exhibit the typical thermal decomposition sequence of biogenic $CaCO_3$, consisting of initial moisture removal, partial decomposition of organic residues, and complete decarbonation to CaO at elevated temperatures. For the uncoated shell powder, mass loss begins gradually at ~200°C and becomes significant between 400–750°C, consistent with progressive decomposition of $CaCO_3$ into CaO and CO_2. The sharp endothermic peak at ~780°C on the DTA curve indicates the main decomposition event of $CaCO_3$, accompanied by a large weight reduction (~40%), which is in line with theoretical CO_2 release. In contrast, the coated oyster shell shows slightly delayed and less abrupt decomposition. Its mass change is more gradual, and the DTA peak is broader and slightly shifted to higher temperature (~800°C), suggesting that the coating modifies the thermal stability of the foaming agent.

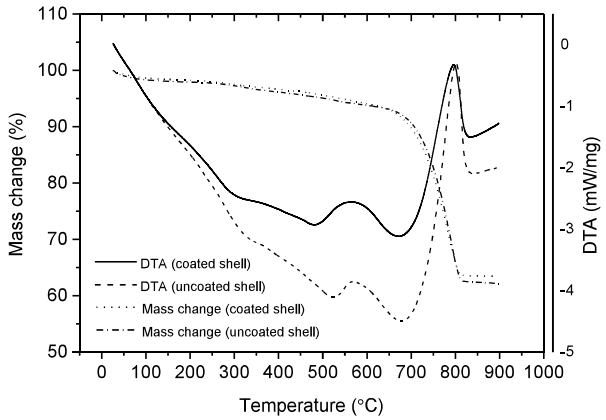

Fig. 2. Thermal analysis of uncoated and coated oyster shell particles.

The macroscopic foam structures of Al samples produced with coated and uncoated oyster shell powders at 3 and 5 wt.% are shown in Fig. 3. At 3 wt.% addition, both coated and uncoated foaming agents were able to generate expanded foams, with the coated powders producing a slightly higher volumetric expansion (216 vol.%) compared to uncoated ones (207 vol.%). The foam cross-sections reveal that the coated powders lead to a more uniform cellular structure with relatively fewer large voids, indicating more controlled gas evolution. In contrast, the uncoated powders result in less uniform pore distribution, with localised regions of pore collapse, which can be attributed to rapid and uncontrolled CO_2 release during decomposition. At 5 wt.% content, the differences between coated and uncoated powders become more pronounced. Both systems achieved higher foam expansion compared to 3 wt.%, with coated powders reaching 238 vol.% and uncoated 230 vol.%.

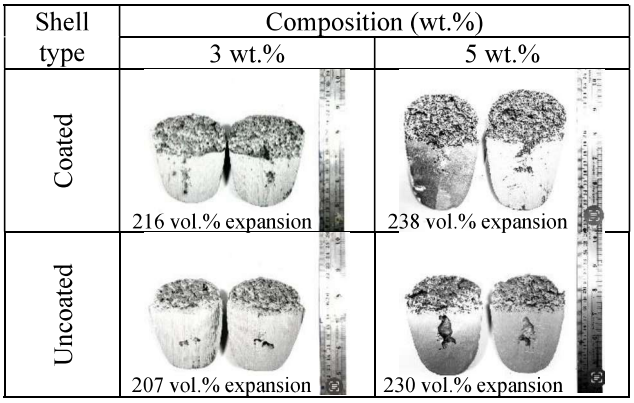

Fig. 3. Cross-section of Al foams samples produced using uncoated and coated oyster shell powders at different contents.

The enhancement in expansion can be attributed to the fluxing effect of NaF, which likely facilitated earlier and more complete decomposition of $CaCO_3$ into CO_2 gas. The coating may also reduce the formation of surface oxides on oyster shell powders, thereby improving the reactivity and wettability between the foaming agent and molten Al [6]. The rapid and controlled gas release contributed to better stabilisation of gas bubbles, leading to more consistent cellular structures.

The optical microstructures of Al foams produced with 5 wt.% coated and uncoated oyster shell powders are shown in Fig. 4. In both cases, the microstructure exhibits a relatively coarse and irregular distribution of eutectic Si particles along with primary Al-rich dendrites. However, the foam produced with NaF-coated oyster shell powder reveals a finer and more uniformly distributed microstructure, with relatively well-dispersed Si particles and fewer large intermetallic agglomerates. The coating appears to stabilise the decomposition of $CaCO_3$, synchronizing the gas release with the increasing viscosity of the ADC12 melt during solidification.

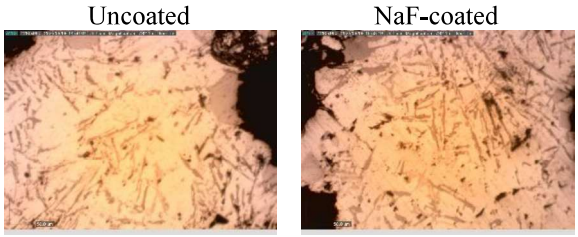

Fig. 4. Optical micrographs showing microstructure of Al foams using uncoated and coated oyster shell particles.

Fig. 5 shows the compressive stress–strain behaviour of Al foams produced with coated and uncoated oyster shell powders at different contents (3 and 5 wt.%). All curves exhibit the typical three-stage deformation behaviour of metallic foams: an initial elastic region with a low slope, followed by a plateau region corresponding to progressive cell wall collapse, and finally a densification stage where stress rises steeply due to pore closure and direct contact between Al ligaments. The plateau stress is significantly affected by both the foaming agent content and the application of surface coating. At 3 wt.%, both coated and uncoated samples exhibit low compressive stress values (~5–15 MPa) across most of the strain range, with little distinction between coated and uncoated powders. This suggests that at low foaming agent content, pore walls remain relatively thin and lack sufficient reinforcement, leading to limited load-bearing capacity regardless of surface treatment.

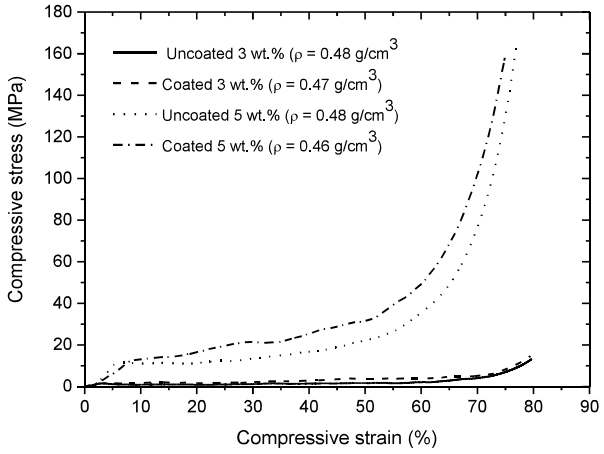

Fig. 5. Compressive behaviour of Al foams samples produced using uncoated and coated oyster shell powders at different contents

In contrast, foams produced with 5 wt.% oyster shell powder demonstrate markedly higher plateau stresses, particularly for the coated powders, which maintain stresses in the range of 20–40 MPa across strains of 20–60%, before entering densification where stresses exceed 150 MPa. This improvement is attributed to both the higher gas evolution at 5 wt.% leading to more uniform pore formation, and the role of the coating layer, which enhances particle dispersion in the melt and delays premature decomposition. These results highlight the dual importance of optimal foaming agent content and surface modification in achieving mechanically robust Al foams.

4 Conclusion

Oyster shell powder is a viable, sustainable foaming agent for ADC12 Al foams via melt route. Surface modification with NaF reduces decomposition onset and enhances foaming efficiency. Foam expansion and compressive properties are strongly influenced by foaming agent content. The 5 wt.% NaF-coated oyster shell powder produced the best results, yielding maximum expansion, uniform pore distribution, and highest plateau stress. Modified biogenic carbonate sources such as NaF-coated oyster shells present a promising eco-friendly alternative to conventional foaming agents.

5 Declaration of competing interest

The authors declare that they have no known competing financial interests or personal relationships that could have appeared to influence the work reported in this paper.

6 Acknowledgment

This research was financially supported by the 90th Anniversary Chulalongkorn University Fund (Ratchadaphiseksomphot Endowment Fund). The authors would also like to acknowledge MetCom for kindly supplying the ADC12 Al ingots used in this study.

7 References

1. J. Banhart, Prog. Mater. Sci. 46 (2001) 559-632. **DOI:** 10.1016/S0079-6425(00)00002-5.
2. F. García-Moreno, Materials. 9 (2016) 85. **DOI:** 10.3390/ma9020085.
3. A. Soloki and M. Esmailian, Metall. Mater. Trans. B. 46 (2015) 1052-1057. **DOI:** 10.1007/s11663-014-0262-1.
4. A. Mirzaei-Solhi et al., Mater. Res. Express. 5 (2018) 096526. **DOI:** 10.1088/2053-1591.
5. J.W. Li et al., IOP. Conf. Ser.: Mater. Sci. Eng. 649 (2019) 012002. **DOI:** 10.1088/1757-899X/649/1/012002.
6. T. Nakamura et al., Mater. Trans. 43 (2002) 1191-1196. **DOI:** 10.2320/matertrans.43.1191.

POSTER SESSION

DAY II — Friday, 21 November 2025 (10:00 - 11:30 AM)

10:10 - 10:20	*(1)*	**A-P-09**	**Dismantling and Cathode Pretreatment of End-of-Life Prismatic Cell Lithium Iron Phosphate Battery** Thanachot Chomnawang *School of Metallurgical Engineering, Suranaree University of Technology*
10:20 - 10:30	*(2)*	**A-P-17**	**Synthesis and Tribological Evaluation of 2D Ni-MOF Additives for Enhanced Lubrication Performance** Sudarat Charoenrumruay *Department of Chemistry, Faculty of science, Kasetsart University*
10:30 - 10:40	*(3)*	**C-P-05**	**Effects of N_2 Flow Rate on the Microstructure of Nanocrystalline TiAlN Films Prepared via Reactive DC Magnetron Co-Sputtering** Adisorn Buranawong *Department of Physics, Faculty of Science, Burapha University*

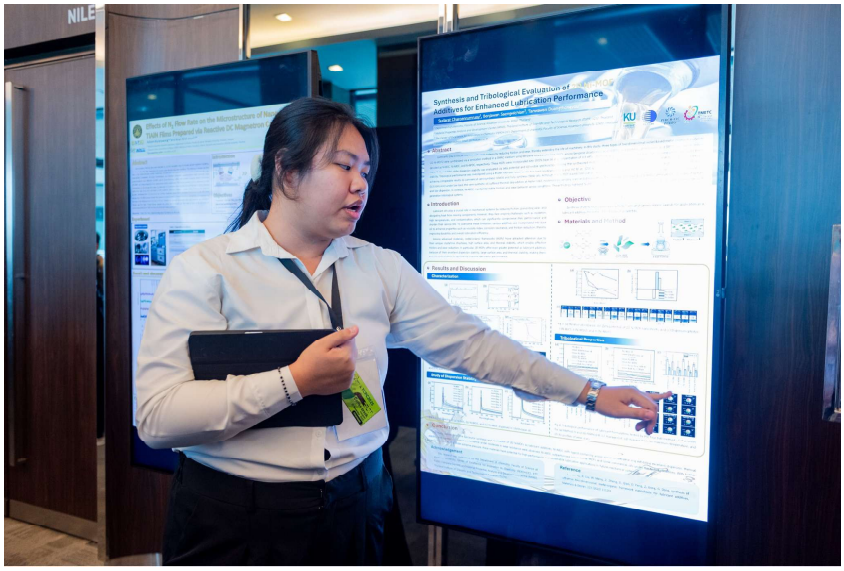

Synthesis and Tribological Evaluation of 2D Ni-MOF Additives for Enhanced Lubrication Performance

Sudarat Charoenrumruay [1], *Benjawan* Saengwichian[2], and *Tanwawan* Duangthongyou[1,3*]

[1]Department of Chemistry, Faculty of Science, Kasetsart University, 10900 Bangkok, Thailand.
[2]Material Properties Analysis and Development Centre (MPAD), Thailand Institute of Scientific and Technological Research (TISTR), 12120 Pathum Thani, Thailand.
[3]The Center of Excellence for Innovation in Chemistry (PERCH-CIC), Department of Chemistry, Faculty of Science, Kasetsart University, 10900 Bangkok, Thailand.
***Corresponding author:** fscitwd@ku.ac.th

Abstract. Lubricants play a crucial role in mechanical systems by reducing friction and wear, thereby extending the life of machinery. In this study, three types of two-dimensional nickel-based metal organic frameworks (2D Ni-MOFs) were synthesized via a sonication method in a DMAC medium using benzene dicarboxylic acid (BDC), amino benzene dicarboxylic acid (ABDC), and biphenyl dicarboxylic acid (BPDC) as organic linkers, denoted as Ni-BDC, Ni-ABDC, and Ni-BPDC, respectively. These MOFs were incorporated into 150SN base oil at a concentration of 0.1 wt%. Structural and morphological characterizations were performed using PXRD, TGA, FT-IR, and SEM, while dispersion stability was evaluated via zeta potential and UV-visible spectroscopy. Among the synthesized material, Ni-ABDC exhibited the highest surface charge and superior dispersion stability. Tribological performance was investigated using a Bruker four-ball tester under two load conditions (147 N and 392 N) at 1200 rpm for 1 h. Ni-ABDC effectively reduced the coefficient of friction at both loads, achieving comparable results to commercial semi-synthetic 10W30 and fully synthetic 5W40 oils. Although the Ni-MOF based formulations exhibited larger wear scar diameters (0.57-0.65 mm) than commercial oils (0.31-0.41 mm) under low load, the semi-synthetic oil suffered thermal degradation at higher load, evidenced by welding scars and discoloration. This sign was also found in Ni-BPDC, attributed to its bulky structure and low dispersion. In contrast, Ni-ABDC maintained stable friction and wear behavior across conditions. These findings highlight Ni-ABDC as a promising, thermally stable, and efficient lubricant additive for next-generation tribological systems.

Graphical abstracts

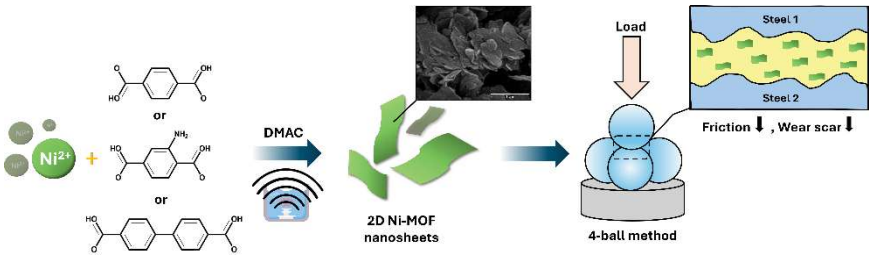

1 Introduction

Lubricant oils play a crucial role in mechanical systems by reducing friction, preventing wear, and dissipating heat from moving components. However, they face ongoing challenges such as oxidation, high temperatures, and contamination, which can significantly compromise their performance and shorten their service life [1-3]. To overcome these limitation, various additives are incorporated into base oil to enhance properties such as viscosity index, corrosion resistance, and friction reduction, thereby improving durability and overall lubrication efficiency [4].

Among advanced materials, metal-organic frameworks (MOFs) have attracted attention due to their unique crystalline structures, high surface area, and thermal stability [5], which enable effective friction and wear reduction [6]. In particular, two-dimensional MOFs (2D MOFs) offer even greater potential as lubricant additives because of their excellent dispersion stability, large surface area, and thermal stability, making them promising candidates to significantly improve lubrication performance [7-9].

2 Experimental procedure

2.1 Synthesis of 2D Ni-MOF nanosheets with varying organic linker

2D Ni-MOF nanosheets were synthesized following a reported method [9] with minor modifications. For Ni-BDC, nickel acetate tetrahydrate (2 g) was dissolved in deionized water (120 mL, solution A), and terephthalic acid (0.5 g) was dissolved in ethanol (120 mL) and N,N-diethylacetamide (120 mL, solution B). Solution A was added to solution B under stirring, followed by sonication for 4 h at room temperature. The product was obtained by centrifugation (5000 rpm for 7 min), washed with deionized water and ethanol, and dried at 60 ºC for 12 h. Ni-ABDC and Ni-BPDC were prepared using similar procedures, employing 2-aminoterephthalic acid and biphenyl dicarboxylic acid, respectively, instead of terephthalic acid.

2.2 Tribological performance evaluation

Lubricant performance was evaluated using a four-ball tester (Bruker UMT TriboLab) in accordance with ASTM D4172, following both Method A and Method B protocols. The tests were performed at a fixed rotational speed of 1200 rpm for 60 minutes using two different loads: 15 kgf (147 N) (Method A) and 40 kgf (392 N) (Method B). All experiments were carried out at ambient room temperature (~25 °C) rather than the standard 75 °C to simulate general operating conditions without active temperature control.

Four identical AISI 52100 steel balls with a diameter of 12.5 mm were used. The upper ball was stationary, while the three lower balls rotated in the lubricant, generating sliding contact. Wear scars were analyzed using a Keyence VR-6000 3D optical profiler, comparing to measurements from a standard 2D optical microscope as specified in ASTM D4172. Each result was averaged from three repeated tests for reliability.

3 Results and Discussion

3.1 Preparation of morphology

The synthesis of a 2D Ni-MOF was carried out using terephthalic acid, a common ligand widely employed in MOF synthesis. Nickel was employed as the metal ion since prior studies examining the influence of various metal ions demonstrated that Ni exhibits superior tribological performance [9, 10]. The ultrasonication method was applied in combination with a solvent capable of forming weak interactions with metal ions, thereby hindering the growth of the crystal framework in three dimensions. Furthermore, the ligand was modified by introducing amino groups onto the benzene ring to enhance the surface charge and consequently improve dispersion stability. In addition, an extra benzene ring was incorporated, which may influence the morphology of the resulting MOF.

3.2 Characterizations of 2D Ni-MOF nanosheets

Fig. 1(a) shows the PXRD patterns of the 2D Ni-MOFs. Ni-BDC, Ni-BPDC, and Ni-ABDC displayed major peaks consistent with previously reported 2D structures [9, 11, 12]. The main diffraction peaks of Ni-BDC and Ni-BPDC shifted to lower angles compared with the 3D structure (JCPDS No. 35-1677) and reported data [13], suggesting increased interlayer spacing in accordance with Bragg's law, likely caused by solvent molecules intercalation within the framework [14]. These findings confirm the successful formation of 2D Ni-MOF nanosheet using different organic linkers. As shown in **Fig. 1(b)**, the IR spectra of all synthesized Ni-MOFs exhibited common vibrational peaks assigned to O–H (adsorbed water), C–H (aromatic), C–H (aliphatic, DMAC), and –COO^- (dicarboxylic acid), with the corresponding vibrational energies summarized in **Table 1.** In addition, Ni-ABDC displayed extra peaks corresponding to N–H stretching from amino functional groups, whereas Ni-BPDC showed characteristic peaks associated with the vibrations of two connected benzene rings. The TGA curves of all synthesized Ni-MOFs revealed multiple stages of weight loss as shown in **Fig. 1(c-e).** The initial step, occurring from room temperature to 100 ºC, corresponded to the removal of surface-adsorbed water and ethanol (Ni-BDC : 3%, Ni-BPDC : 5.5%, Ni-ABDC : 5%). The subsequent decomposition from 100 to 220 ºC was attributed to surface-bound DMAC, followed by further decomposition between 220 to 360 ºC, which was assigned to DMAC molecules intercalated between the 2D layers (Ni-BDC : 7% and 6%, respectively). In the cases of Ni-ABDC and Ni-BPDC, this decomposition process occurred continunuosly from 100 to 360 ºC (Ni-BPDC : 9%, Ni-ABDC : 13%). The final weight loss stage, observed between 400 and 500 °C, was associated with the decomposition of the MOF framework due to the breakdown of the organic linkers. These results indicate that the synthesized 2D Ni-MOFs possess relatively high thermal stability, making them suitable for applications

involving elevated temperatures. The TGA analysis indicated that only a small amount of DMAC (approximately 3–6%) was intercalated between the layers of the 2D Ni-MOFs, which implies that DMAC is weakly retained within the framework. Consequently, this weaker interaction likely increases the surface energy of the nanosheets, thereby promoting a higher degree of sheet restacking compared with the other Ni-MOFs [15, 16]. SEM images as shown in **Fig. 1(f-top)** revealed nanosheet-like morphologies of the Ni-MOFs synthesized with different ligands. To observe the true morphology and actual size of the nanosheets, a surfactant was added to prevent aggregation. Although BDC- and ABDC-based MOFs exhibited relatively similar nanosheet morphologies, slight differences in thickness and packing density were observed. The Ni-BDC nanosheets had an average thickness of about 35 nm, whereas the Ni-ABDC nanosheets were slightly thinner (≈30 nm) and tended to pack more densely. In contrast, the BPDC-based MOF formed smaller nanosheets, which aggregated into more compact assemblies with an average thickness of about 40 nm. This pronounced aggregation in Ni-BPDC is likely attributed to the larger size of the biphenyl linker, which promotes stronger π–π interactions and facilitates restacking of the 2D sheets compared with the smaller BDC- and ABDC-based linkers. The nanosheet morphologies observed by SEM were in good agreement with the TGA results. In the case of Ni-BPDC, TGA analysis revealed relatively low DMAC content, indicating that fewer DMAC molecules were intercalated between the 2D layers. As a result, the weaker interaction between DMAC and the framework likely increased the surface energy of the nanosheets, promoting stronger sheet–sheet interactions. This higher surface energy is consistent with the pronounced aggregation and denser restacking of the Ni-BPDC nanosheets compared with Ni-BDC and Ni-ABDC. These observations suggest that the extent of DMAC intercalation plays a key role in controlling the dispersion and stacking behavior of 2D Ni-MOF nanosheets. EDS analysis confirmed the elemental distribution within the MOF structures, showing the presence of C, O, N (from DMAC), and Ni in all samples shown in **Fig. 1(f-bottom)**. Notably, Ni-ABDC contained a higher nitrogen content due to the amino groups in the aminoterephthalic acid linker.

Table 1. Functional groups of 2D Ni-MOF nanosheets.

Functional groups (cm^{-1})			
	Ni-BDC	Ni-BPDC	Ni-ABDC
O-H group	3569	3615	3670
C-H aromatic	3000-3100		
C-H aliphatic	2800-3000		
Asymmetric and symmetric of -COO^- group	1557 and 1376	1591 and 1362	1557 and 1376
Benzene ring	1506, 1155 and 1028	1536, 1189 and 1002	1500, 1168 and 1052
Ring deformation of benzene ring	-	764	-
N-H group	-	-	3333

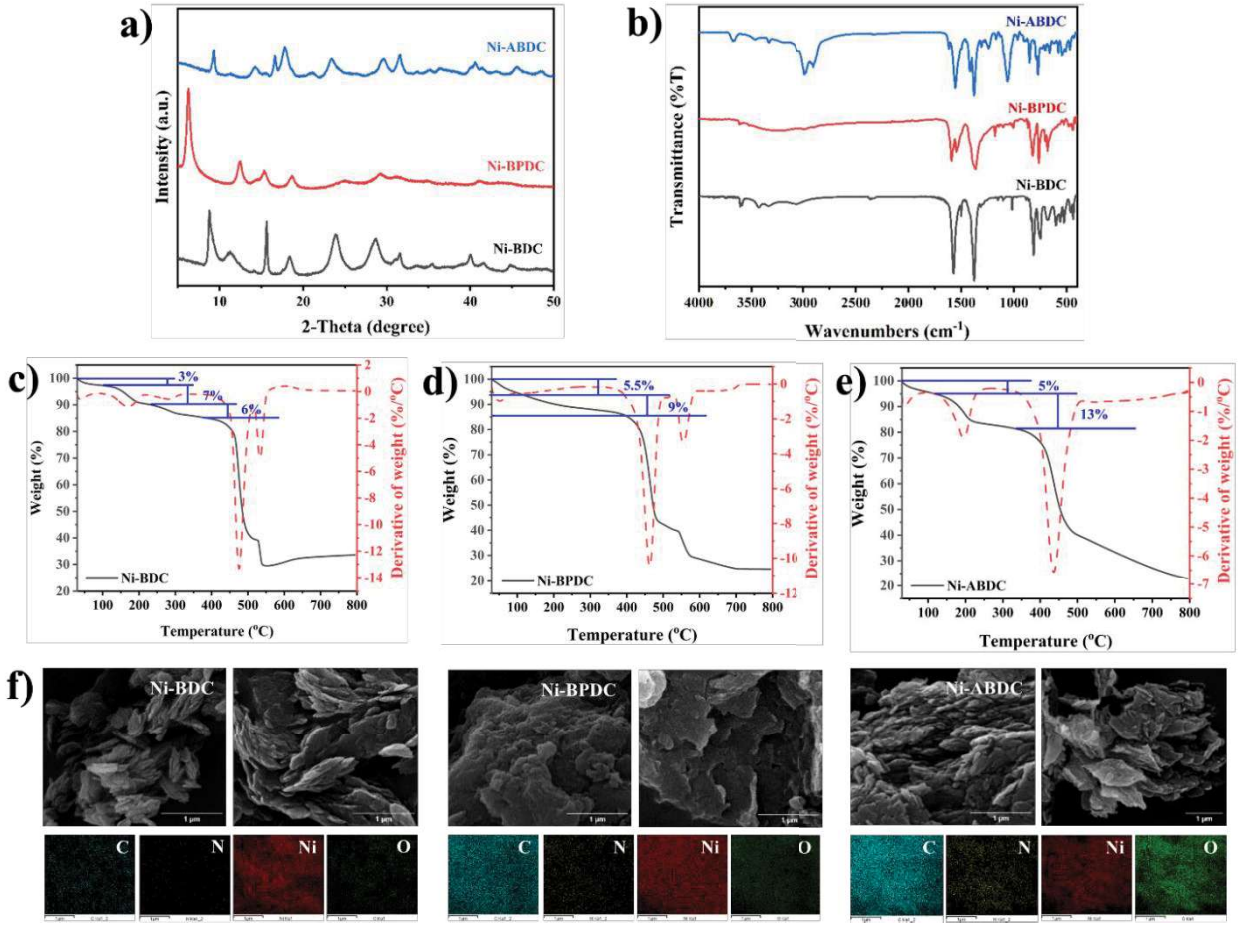

Fig. 1. Characterization of 2D Ni-MOFs nanosheets ; PXRD patterns (a), FTIR spectra (b), TGA curves of Ni-BDC (c), Ni-BPDC (d) and Ni-ABDC (e), and SEM images (f-top) without Tween80 (left), with Tween80 (right) and EDS mapping (f-bottom).

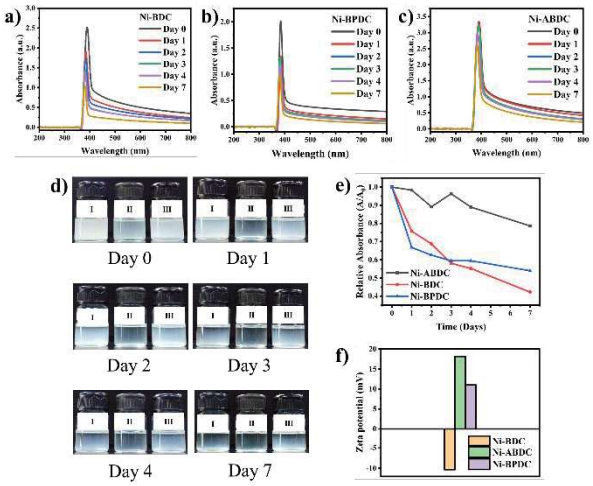

Fig. 2. UV-vis spectra of Ni-BDC (a), Ni-BPDC (b), and Ni-ABDC (c) dispersed in 150SN base oil. Dispersion photos (d) ; I (Ni-BDC), II (Ni-BPDC), and III (Ni-ABDC). Relative absorbance (e) and Zeta potential (f) of 2D Ni-MOF nanosheets.

3.2 Dispersion stability

As shown in **Fig. 2(a-c)**, all Ni-MOFs dispersed in 150SN base oil exhibit an absorption peak around 385 nm, with the absorbance gradually decreasing over time at room temperature. Based on visual observation and the relative absorbance shown in **Fig. 2(d-e)**, the dispersion stability followed the order Ni-ABDC > Ni-BDC > Ni-BPDC, with Ni-ABDC maintaining the most stable absorbance over time. This superior dispersibility of Ni-ABDC-C in base oil is further supported by its highest zeta potential (**Fig. 2(f)**), indicating stronger electrostatic repulsion compared with the other Ni-MOFs. These results are consistent with the proposed hypothesis that introducing amino groups into the benzene ring can enhance the dispersion stability of Ni-MOFs in oil.

3.3 Tribological properties

Fig. 3(a-f) shows the tribological characteristics of the lubricant formulations under varying load conditions. At low loads, all lubricants exhibited stable coefficients of friction (CoF). The Ni-ABDC shows the lowest average CoF, approximately 50% lower than other Ni-MOFs, indicating superior friction-reducing capability. No thermal degradation or surface welding was observed. Although wear scar diameters (WSDs) were approximately 30% higher than those of fully synthetic oil due to base oil 150SN limitations, Ni-ABDC maintained a clear advantage in friction performance. At higher loads, both Ni-BPDC and semi-synthetic 10W30 oil exhibited unstable CoF behavior. A sharp decrease in CoF was observed beyond approximately 50 °C, likely due to the effect of elevated temperature on the lubricant film. During testing, abnormal machine noise indicated direct metal-to-metal contact between the upper and lower balls. Post-test inspection revealed black oxide residues in the oil and dark blue discoloration of the ball surfaces, corresponding to tempering colors of steel at contact temperatures exceeding 550 °C, suggesting thermal degradation of the Ni-BPDC-based lubricant. These effects are possibly associated with Ni-BPDC's bulky molecular structure and poor dispersion, which caused localized welding. Similar failure behavior was observed in the semi-synthetic 10W30 lubricant. In contrast, Ni-ABDC maintained stable CoF and minimal surface damage, despite having similar WSDs to those of Ni-BDC and the base oil. Its amino-functionalized ligand likely enhances dispersion and interfacial bonding, facilitating the formation of a stable protective tribofilm across the tested load range.

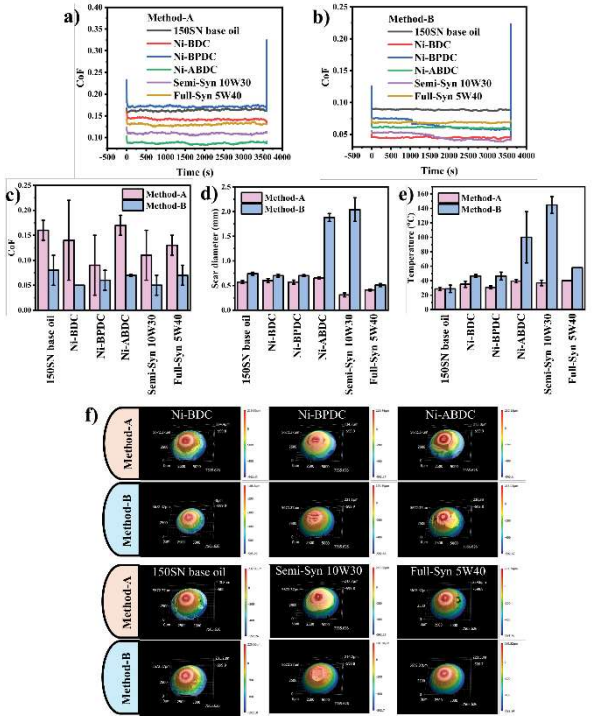

Fig. 3. Tribological performance of lubricant formulations tested by the four-ball method : CoF profiles for Method A (a) and Method B (b), Average CoF (c), Average WSD (d), maximum temperature (e), and 3D profiles of wear scars (f).

4 Conclusion

This study demonstrates the successful synthesis and application of 2D Ni-MOFs as lubricant additives, Ni-ABDC with ligand containing amino group on benzene ring exhibiting excellent dispersion, thermal stability, and superior tribological performance under moderate load conditions. Although slight compromises in wear resistance were observed, Ni-ABDC outperformed conventional MOFs and some commercial oils under the tested conditions. With further optimization and testing under extreme pressure, these materials have potential for high-performance and sustainable lubrication applications in future mechanical systems.

5 Acknowledgement

This research was supported, by the Department of Chemistry, Faculty of Science at Kasetsart University, Center of Excellence for Innovation in Chemistry (PERCH-CIC), PTT Public Company Limited, and Material Properties Analysis and Development Centre (MPAD), Thailand Institute of Scientific and Technological Research (TISTR).

6 References

1. S. Zhu, J. Cheng, Z. Qiao, J. Yang, High temperature solid-lubricating materials: A review, Tribology International, 133 (2019) 206-223. **DOI:** 10.1016/j.triboint.2018.12.037
2. Y. Wu, W. Li, M. Zhang, X. Wang, Oxidative degradation of synthetic ester and its influence on tribological behavior, Tribology International, 64 (2013) 16-23. **DOI:** 10.1016/j.triboint.2013.02.002
3. A. Al Sheikh Omar, F.M. Salehi, U. Farooq, A. Morina, Additives Depletion by Water Contamination and Its Influences on Engine Oil Performance, Tribology Letters, 72 (2024) 74. **DOI:** 10.1007/s11249-024-01876-y
4. M. Gulzar, H.H. Masjuki, M.A. Kalam, M. Varman, N.W.M. Zulkifli, R.A. Mufti, R. Zahid, Tribological performance of nanoparticles as lubricating oil additives, Journal of Nanoparticle Research, 18 (2016) 223. **DOI:** 10.1007/s11051-016-3537-4
5. L.P.L. Mosca, A.B. Gapan, R.A. Angeles, E.C.R. Lopez, Stability of Metal–Organic Frameworks: Recent Advances and Future Trends, Engineering Proceedings, 56 (2023) 146. **DOI:** 10.3390/ASEC2023-16280
6. C. Wang, M. Zhou, H. Cao, H. Lin, S. Han, Recent advances in metal–organic frameworks for lubrication, Molecular Systems Design & Engineering, 9 (2024) 243-253. **DOI:** 10.1039/D3ME00149K
7. F.-F. Wang, G. Tan, H. Ding, Z. Liu, Z.-L. Cheng, Novel fabrication for 2D MOFs-based oil-in-water lubricating emulsion via the self-assembly interface, Materials Letters, 297 (2021) 129981. **DOI:** 10.1016/j.matlet.2021.129981
8. M. Zhao, Y. Huang, Y. Peng, Z. Huang, Q. Ma, H. Zhang, Two-dimensional metal–organic framework nanosheets: synthesis and applications, Chemical Society Reviews, 47 (2018) 6267-6295. **DOI:** 10.1039/C8CS00268A
9. H. Yu, X. Liu, W. Meng, Z. Zheng, D. Qiao, D. Feng, Z. Gong, G. Dong, Synthesis of ultrathin two-dimensional metal-organic framework nanosheets for lubricant additives, Materials & Design, 223 (2022) 111251. **DOI:** 10.1016/j.matdes.2022.111251
10. S. Charoenrumruay, T. Duangthongyou, *Enhanced Tribological Properties of Lubricants Using Modified 2D Ni-MOF Nanosheets as Lubricant Additives*, in Proceeding of Pure and Applied Chemistry International Conferences (PACCON 2025), Bangkok, Thailand, February 13-15 (2025), 503-508.
11. C. Meng, Y. Cao, Y. Luo, F. Zhang, Q. Kong, A.A. Alshehri, K.A. Alzahrani, T. Li, Q. Liu, X. Sun, A Ni-MOF nanosheet array for efficient oxygen evolution electrocatalysis in alkaline media, Inorganic Chemistry Frontiers, 8 (2021) 3007-3011. **DOI:** 10.1039/D1QI00345C
12. Z. Jun, M. Xiaosi, Z. Jujiao, X. Yin, T. Yanzong, Nickel-based metal-organic-frameworks as electrocatalysts for electrochemical oxidation of ammonia, Applied and Computational Engineering, 70 (2024) 92-101. **DOI:** 10.54254/2755-2721/70/20240962
13. F. He, N. Yang, K. Li, X. Wang, S. Cong, L. Zhang, S. Xiong, A. Zhou, Hydrothermal synthesis of Ni-based metal organic frameworks/graphene oxide composites as supercapacitor electrode materials, Journal of Materials Research, 35 (2020) 1439-1450. **DOI:** 10.1557/jmr.2020.93
14. S. Gao, Y. Sui, F. Wei, J. Qi, Q. Meng, Y. He, Facile synthesis of cuboid Ni-MOF for high-performance supercapacitors, Journal of Materials Science, 53 (2018) 6807-6818. **DOI:** 10.1007/s10853-018-2005-1
15. Y. Wang, J. Ma, F. Jin, T. Li, N. Javanmardi, Y. He, G. Zhu, S. Zhang, J.-D. Xu, T. Wang, Z.-Q. Feng, Recent Advances in the Synthesis and Application of Monolayer 2D Metal-Organic Framework Nanosheets, Small Science, 4 (2024) 2400132. **DOI:** 10.1002/smsc.202400132
16. P. Wang, C. Yang, J. Yao, H. Li, Z. Hu, Z. Li, Two-dimensional metal organic framework nanosheets in electrocatalysis, Chemical Science, 16 (2025) 6583-6597. **DOI:** 10.1039/D5SC01390A

POSTER SESSION

DAY II		Friday, 21 November 2025 (10:00 - 11:30 AM)	
10:10 - 10:20	*(1)*	**A-P-09**	**Dismantling and Cathode Pretreatment of End-of-Life Prismatic Cell Lithium Iron Phosphate Battery** Thanachot Chomnawang *School of Metallurgical Engineering, Suranaree University of Technology*
10:20 - 10:30	*(2)*	**A-P-17**	**Synthesis and Tribological Evaluation of 2D Ni-MOF Additives for Enhanced Lubrication Performance** Sudarat Charoenrumruay *Department of Chemistry, Faculty of science, Kasetsart University*
10:30 - 10:40	*(3)*	**C-P-05**	**Effects of N_2 Flow Rate on the Microstructure of Nanocrystalline TiAlN Films Prepared via Reactive DC Magnetron Co-Sputtering** Adisorn Buranawong *Department of Physics, Faculty of Science, Burapha University*

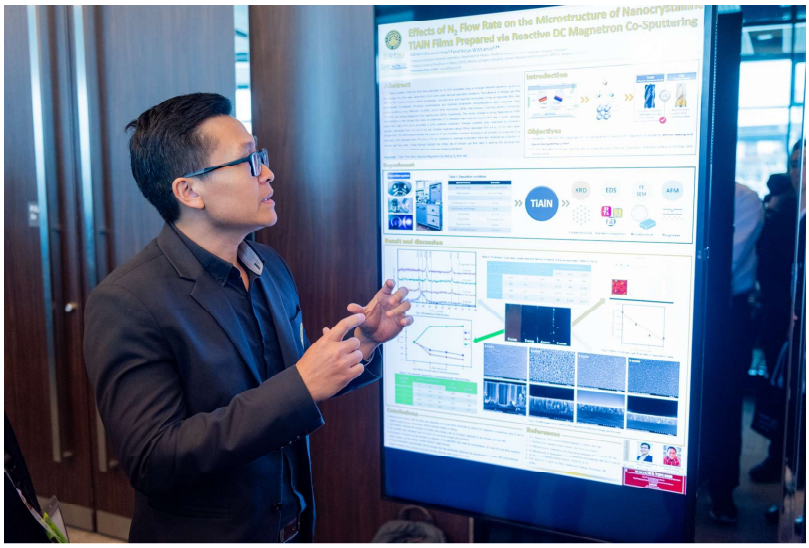

Effects of N_2 Flow Rate on the Microstructure of Nanocrystalline TiAlN Films Prepared via Reactive DC Magnetron Co-Sputtering

Adisorn Buranawong [1,2], and *Nirun* Witit-anun[1,2*]

[1]Department of Physics, Faculty of Science, Burapha University, Chonburi, 2013, Thailand.
[2]Thailand Center of Excellence in Physics (ThEP), Ministry of Higher Education, Science, Research and Innovation (MHESI), Bangkok, 10400, Thailand.
***Corresponding author:** nirun@buu.ac.th

Abstract. Nanocrystalline TiAlN thin films were deposited on Si (100) substrates using a co-target reactive magnetron sputtering, with nitrogen (N_2) flow rates varied from 0 to 6 sccm under identical deposition conditions. The influence of nitrogen gas flow rates on the crystal structure, surface morphology, microstructure, and chemical composition of the as-deposited films was systematically investigated. Structural, morphological, and chemical composition characterizations were conducted using grazing-incidence X-ray diffraction (GI-XRD), atomic force microscopy (AFM), field emission scanning electron microscopy (FE-SEM), and energy-dispersive X-ray spectroscopy (EDS), respectively. The results revealed a strong dependence of film characteristics on the nitrogen flow rates. A preferential (111) orientation was observed at a low flow rate (2 sccm), whereas higher flow rates (4–6 sccm) promoted a (200) preferred orientation. Average crystallite sizes, estimated by Scherrer's equation, decreased from 12.3 nm to 9.2 nm. Surface roughness values (Rrms) decreased from 4.4 to 1.9 nm with higher nitrogen flow. FE-SEM analysis showed the presence of nanocrystalline columnar structures in all samples, accompanied by a decrease in film thickness from 575 nm to 170 nm. Variations in chemical composition were also observed as a function of nitrogen gas flow rates. These findings highlight the critical role of nitrogen gas flow rates in tailoring the structural and morphological features of TiAlN thin films for advanced coating applications.

Graphical abstracts

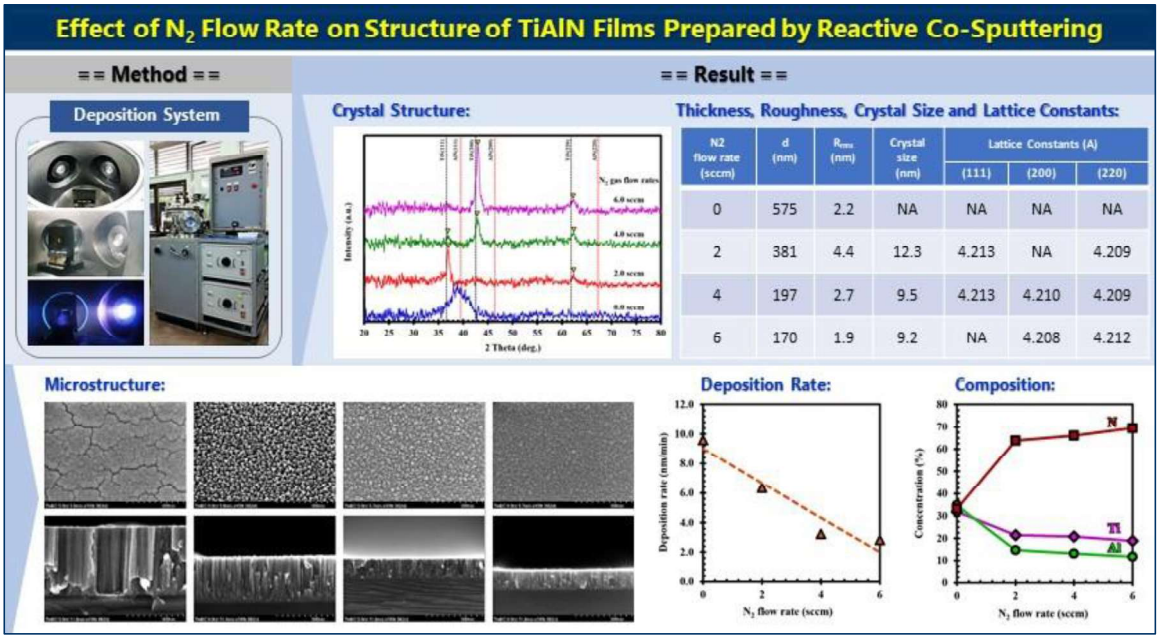

1 Introduction

Over the past decade, the advancement of industrial applications has increased the demand for improved surface performance in machinery and tooling. A key focus in surface engineering is the development of materials with enhanced tribological behavior, notably low friction and wear resistance under varying conditions. Transition metal nitride hard coatings represent one of the most effective solutions for meeting these demands.

Binary transition metal nitrides such as TiN, CrN, and ZrN represent the first generation of hard coatings, offering greater hardness than conventional of coatings on tool materials but suffering from thermal oxidation at high temperatures [1,2]. To overcome these drawbacks, ternary nitride coatings such as TiAlN, TiZrN, TiVN, and TiCrN have been developed, with TiAlN receiving the most attention for its superior hardness, low friction, and excellent resistance to oxidation and wear [3,4].

TiAlN thin films have been synthesized using various techniques, such as sputtering, cathodic arc, and ion beam-assisted deposition [5]. Among these, sputtering is particularly attractive due to its low processing temperature, use of non-toxic gases, and relatively simple operation [6]. It is well known that films deposited by the same technique often exhibit different properties due to variations in system and deposition conditions, which influence film structures; thus, understanding the effects of deposition parameters remains essential. Although substrate heating and biasing are commonly applied to improve TiAlN film, which increase costs and induce thermal effects, making them unsuitable for thermally sensitive materials, thereby highlighting the importance of investigating sputter deposition without heating or biasing.

In the present work, the effects of nitrogen flow rates on the structures of TiAlN thin films deposited at room temperature by reactive DC magnetron co-sputtering without heating and bias at low sputtering current. The crystal structure, thickness, surface morphology, and microstructure were analyzed as a function of nitrogen gas flow rate investigated and discussed.

2 Experimental procedure

TiAlN thin films were deposited on Si substrates using a reactive DC magnetron sputtering technique. The deposition was carried out in a cylindrical SUS304 vacuum chamber, achieving a base pressure below 5×10^{-5} mbar. An unbalanced magnetron configuration was employed, with planar and central magnets mounted on the target backing plate, generating magnetic fields of approximately 1000 G and 1400 G, respectively. Sputtering was powered by a variable DC supply of up to 1000 V and 3 A, enabling precise control of the deposition process.

Before deposition, the coating chamber was evacuated to a base pressure of 5×10^{-5} mbar. The TiAlN films were deposited at different nitrogen gas flow rates from 0 sccm to 6 sccm, while deposition parameters such as substrate-target distances, Ar gas flow rate, sputtering current, substrate temperature and working pressure were constant. The deposition parameters are summarized in Table 1.

The crystal structure and crystallite size of the TiAlN thin films were analyzed using glancing incidence X-ray diffraction (GIXRD; BRUKER D8) with Cu Kα radiation (λ = 0.154 nm). XRD patterns were recorded in a continuous 2θ scanning mode at a rate of 2°/min, with a grazing incidence angle of 3°. The film phases were identified based on Bragg's law and compared with the Joint Committee on Powder Diffraction Standards (JCPDS) database. Crystallite sizes were estimated using the Scherrer equation. Film thickness, microstructure, and cross-sectional morphology were examined by field emission scanning electron microscopy (FE-SEM; Hitachi S4700). The chemical composition of the as-deposited TiAlN films was determined by energy dispersive X-ray spectroscopy (EDS; EDAX) coupled with scanning electron microscopy (SEM; LEO 1450VP).

Table 1. Thin films deposition conditions.

Parameters	Details
Sputtering target	Ti (99.95%) Al (99.95%)
Temperature	room temperature
Target to substrate distance	130 mm
Base pressure	5.0×10^{-5} mbar
Working pressure	5.0×10^{-3} mbar
sputtering power of Ti target	220 W
sputtering power of Al target	75 W
Ar flow rate	16 sccm
N_2 flow rates	0,2,4, 6 sccm
Deposition time	60 min

3 Results and Discussion

3.1 Deposition rate

TiAlN thin films were successfully deposited on Si and glass slides substrates (Figure 1) using reactive DC unbalanced magnetron co-sputtering under varying nitrogen flow rates, while other deposition parameters were kept constant. As shown in Figure 2, the deposition rate, determined from film thickness over deposition time, decreased from 9.6 nm/min to 2.8 nm/min as the nitrogen flow increased from 0 to 6 sccm. This reduction is attributed to target poisoning, where nitrogen reacts with the target surface to form a thin nitride layer, thereby suppressing the sputtering rate—a phenomenon widely reported as the primary cause of reduced deposition efficiency in reactive sputtering processes

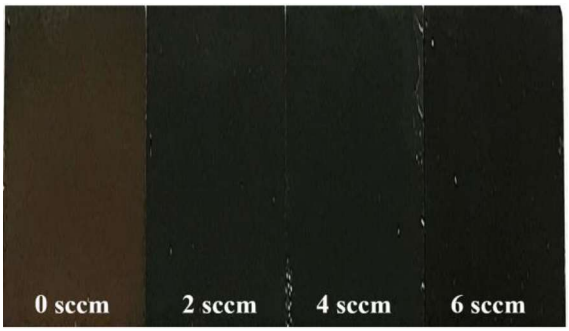

Fig. 1. Features of TiAlN films deposited on glass substrates

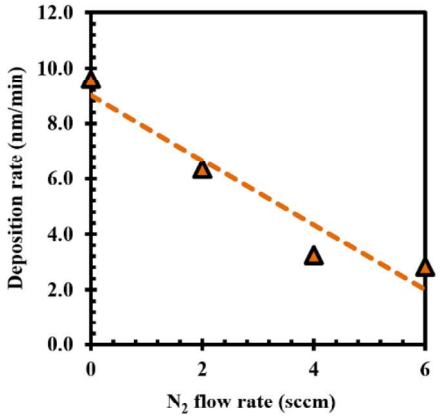

Fig. 2. Effect of nitrogen gas flow rate on deposition rates.

3.2 Chemical composition

The chemical composition of the as-deposited TiAlN thin films was analyzed using EDS, as summarized in Table 2. As the nitrogen gas flow rates increased from 0 to 6 sccm, the Ti and Al contents remained constant (18.8-31.9 at.% and 11.7-34.8 at.%, respectively), while the N content increased from 33.3 to 69.5 at.% (Figure 2). In this work the film composition, expressed as $Ti_xAl_{1-x}N_y$ with x=Ti/(Ti+Al) and y=N/(Ti+Al), showed that Ti content remained stable at 0.48–0.62 across all nitrogen gas flow rates, whereas N content increased with higher N_2 flow rates. The N-to-metal ratio (y) exceeded 1, indicating that all of the films in this work were over stoichiometry.

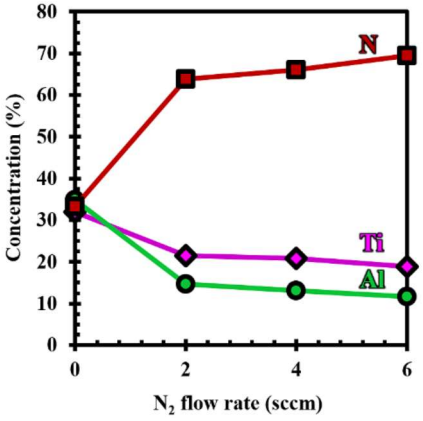

Fig. 3. Effect of N_2 flow rates on chemical composition.

Fig. 2. The chemical composition of the as-deposited TiAlN thin films.

N_2 flow rate (nm)	Chemical composition (at.%(			x= Ti/(Ti+Al)	y= N/(Ti+Al)
	Ti	Al	N		
0	31.9	34.8	33.3	0.48	0.50
2	21.5	14.6	63.9	0.60	1.77
4	20.8	13.1	66.1	0.61	1.95
6	18.8	11.7	69.5	0.62	2.27

3.3 Crystal structure

Figure 3 showed the XRD patterns of the as-deposited TiAlN thin films deposited on Si substrates with different the nitrogen gas flow rate from 0 sccm to 6 sccm. The standard 2θ positions for the (111), (200), and (220) of the TiN and AlN structure were included for comparison purposes. The XRD pattern revealed that the films exhibited diffraction pattern at 2θ of 36.93^O, 42.93^O – 42.95^O, and 62.30^O – 62.35^O which according to (111), (200), and (220) planes of the Face-centered cubic (FCC) TiAlN structures.

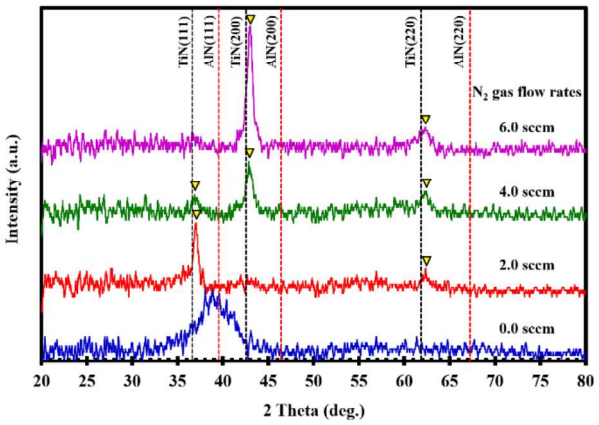

Fig. 4. XRD patterns of TiAlN thin films.

The XRD patterns of TiAlN thin films deposited on glass slide substrates at different nitrogen gas flow rates (0.0-6.0 sccm) are presented in Figure 4. At a nitrogen flow rate of 0.0 sccm, the diffraction pattern exhibits broad and weak peaks, indicating a poorly crystallized structure or an amorphous-like phase due to insufficient nitrogen incorporation during deposition process. With the introduction of nitrogen gas flow rates at 2.0 sccm, distinct diffraction peaks corresponding to TiAlN(111) and TiAlN(220) planes emerge, suggesting the formation of a crystalline TiN phase.

As the nitrogen gas flow rate increases further to 4.0 sccm, the TiAlN(200) peak becomes more pronounced, reflecting enhanced crystallinity and preferential orientation along the (200) plane. This behavior is commonly observed in TiN-based coatings deposited by reactive sputtering, where increased nitrogen gas supply promotes stoichiometric TiN formation and grain growth. In addition, weak reflections of TiAlN(111) and TiAlN(200) appear, confirming the incorporation of Al atom into the nitride lattice of the as-deposited thin film.

At the highest nitrogen gas flow rate of 6.0 sccm, the XRD pattern shows broadened peaks and reduced intensity of TiN(200), which may be attributed to target poisoning effects and over-saturation of nitrogen during sputtering. Excessive nitrogen often leads to decreased deposition rate and the formation of fine-grained or partially amorphous phases. The appearance of TiAlN related peaks at this condition suggests a competitive phase formation between TiN and AlN, which can hinder the growth of highly crystalline TiN.

Overall, the results indicate that nitrogen gas flow rate plays a critical role in determining the crystallinity, phase composition, and preferred orientation of TiAlN thin films. An intermediate flow rate (2.0–4.0 sccm) appears optimal for obtaining well-crystallized TiAlN(200)-oriented films with Al incorporation, while too low or too high nitrogen supply results in poor crystallinity or secondary phase dominance. These observations are consistent with previous reports on TiAlN coatings prepared by reactive magnetron sputtering, where the balance of metal and nitrogen flux is crucial for tailoring microstructure and phase stability. This result show that, in this work, the preferential orientation of the as-deposited film varies with the nitrogen gas flow rate.

The average crystal sizes of the as-deposited films decreased from 12.3 nm to 9.2 nm with increasing nitrogen gas flow rate (Table 3), as calculated from the FWHM of XRD peaks using Scherrer's equation. This reduction can be explained by the effect of higher nitrogen incorporation, which increases nucleation sites while limiting grain growth due to reduced surface diffusion and possible target poisoning. As a result, the crystallites become finer, leading to the broadening of XRD peaks observed at higher nitrogen flow rates. Such grain refinement is significant because it may enhance hardness through the Hall–Petch effect, although it can simultaneously increase residual stress or decrease the degree of crystallinity. Therefore, controlling nitrogen gas flow rates is an important factor not only for phase formation but also for tailoring the microstructure and performance of TiAlN coatings.

Fig. 3. Thickness, roughness, crystal size and lattice constants of the as-deposited TiAlN thin films.

N_2 flow rate (nm)	Thickness (nm)	Rrms (nm)	Crystal size (nm)	Lattice constant (Å)		
				(111)	(200)	(220)
0	575	2.2	NA	NA	NA	NA
2	381	4.4	12.3	4.213	NA	4.209
4	194	2.7	9.5	4.213	4.210	4.209
6	170	1.9	9.2	NA	4.208	4.212

3.4 Microstructure

Figure 4 showed the FE-SEM microstructure and the cross-sectional images of the TiAlN thin films deposit with different the nitrogen gas flow rate. The nanocrystalline TiAlN grains were formed mainly of individual grain and compact pattern which are clearly identified from low nitrogen gas flow rate (2 sccm). When the nitrogen gas flow rate increased to 6 sccm, it was found that the surface composed of small nano grains size with less void and denser structure. The as-deposited films exhibited smoothing surface with increasing of the nitrogen gas flow rate, corresponded to decreased crystallite size which determined from XRD pattern.

From cross-section analysis were clearly identified that thickness was decreased from 575 nm to 170 nm resulting from the target poisoning and decreased of mean free path as the nitrogen gas flow rates increased. The cross-section observation apparently revealed the equiaxial structure with also exhibited good columnar pattern. As the nitrogen gas flow rates increased, bombarding with higher energetic particles lead to the microstructure with densely packed fibrous grains which correspond to Zone T in the structure Thornton's zone model.

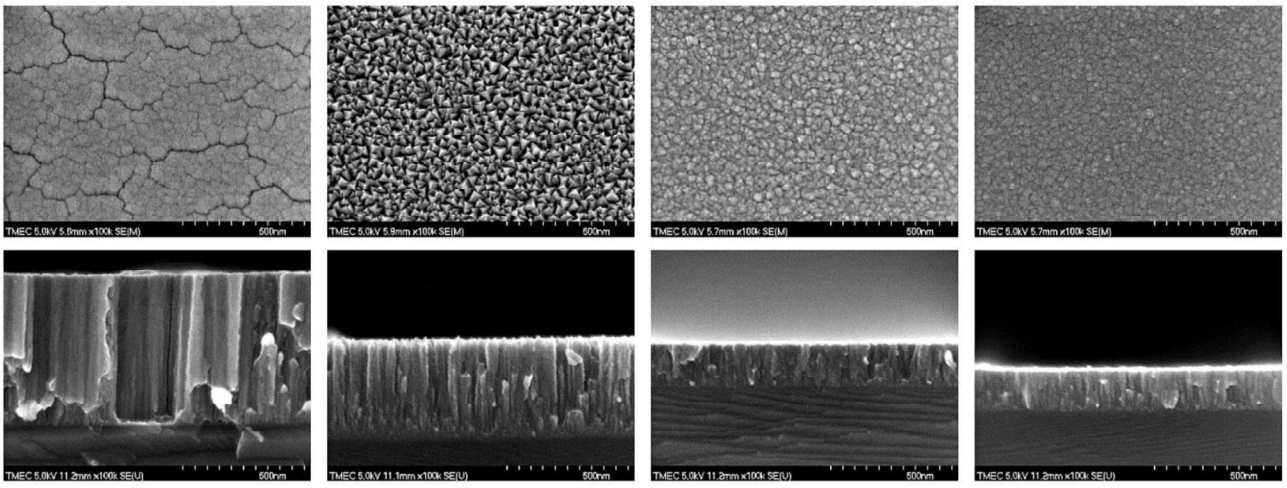

(a) N_2 = 0 sccm (b) N_2 = 2 sccm (c) N_2 = 4 sccm (d) N_2 = 6 sccm

Fig. 5. FE-SEM images of the TiAlN thin films deposited at difference nitrogen gas flow rates.

4 Conclusion

In this work, nanostructured ternary TiAlN thin films were deposited onto Si and glass substrates by reactive DC magnetron co-sputtering using Ti and Al metallic targets at room temperature, without substrate heating or biasing. The as-deposited films consistently exhibited TiAlN solid solutions with an fcc phase across all nitrogen gas flow rates. An increase in nitrogen flow rate resulted in a reduction of the deposition rate, while the concentrations of Ti and Al in the films remained nearly constant, and the nitrogen content showed a slight increase. The nitrogen-to-metal ratio exceeded unity, indicating that all deposited films were over-stoichiometric. XRD analysis confirmed the formation of (Ti,Al)N solid solutions with an fcc phase, and revealed that the preferred orientation of the films depended on the nitrogen gas flow rate. The crystallite sizes decreased from 12.3 nm to 9.2 nm as the nitrogen flow increased, whereas both lattice constants and film thickness were found to increase. Furthermore, FE-SEM observations demonstrated that the nitrogen flow rate significantly influenced the microstructural evolution, with cross-sectional images revealing dense columnar structures.

5 References

1. W.L. Wang et al., Diamond and Related Materials. 9 (2000) 1660-1663.
2. L. Xuechao et al., Applied Surface Science. 256 (2010) 4272-4279.
3. N. Witit-anun and A. Teekhaboot, Key Engineering Materials. 675-676(2016) 181-184.
4. N. Witit-anun and A. Buranawong, Applied Mechanics and Materials. 866 (2017) 318-321.
5. W. Zhou et al., Applied Surface Science. 313(2014) 10-18.
6. P.W. Shum, K.Y. Li and Y.G. Shen, Surface and Coatings Technology. 198 (2004) 414-419.

Type text here